Research Square

Preprints are preliminary reports that have not undergone peer review.
They should not be considered conclusive, used to inform clinical practice,
or referenced by the media as validated information.

Efficient Utilization of Lithium Slag: Grinding Properties of Lithium Slag and the Hydration Mechanism of Lithium Slag-Cement Cementitious Materials

Kaifan ZHANG
Jiangxi University of Science and Technology
Xiaojun WANG
Jiangxi University of Science and Technology
Changlong WANG
baistuwong@139.com

Hebei University of Engineering
Tianyong HUANG
Beijing Building Materials Academy of Sciences Research
Yunyi BAI
Hebei University of Engineering

Research Article

Keywords: Lithium Slag, cementitious materials, grinding aids, triethanolamine, diethylene glycol

Posted Date: November 2nd, 2026

DOI: https://doi.org/10.21203/rs.3.rs-11188670/v1

License: This work is licensed under a Creative Commons Attribution 4.0 International License.
Read Full License

Additional Declarations: No competing interests reported.

Efficient Utilization of Lithium Slag: Grinding Properties of Lithium Slag and the Hydration Mechanism of Lithium Slag-Cement Cementitious Materials

Kaifan ZHANG[1,2], Xiaojun WANG[1,2*], Changlong WANG[3*], Tianyong HUANG[4], Yunyi BAI[3]

(1. Jiangxi Provincial Key Laboratory of Safe and Efficient Mining of Rare Metal Resource, Ganzhou 341000*, PR China;*

2. School of Mining Engineering, Jiangxi University of Science and Technology, Ganzhou 341000, PR China;

3.Hebei Province Key Laboratory for Low-Carbon Construction and Resilience Enhancement of Construction Engineering, School of Civil Engineering, Hebei University of Engineering, Handan 056038*, PR China;*

4. Beijing Building Materials Academy of Sciences Research, State Key Laboratory of Materials Low-Carbon Recycling, Beijing 100041, PR China

Corresponding author: Changlong WANG, E-mail: baistuwong@139.com.

Abstract: In order to enhance the hydration activity of lithium slag (LS) in cementitious materials. Three grinding aids (GAs)， including ethylene glycol (EG), triethanolamine (TEA), and sodium tripolyphosphate (STPP), are added during mechanical grinding to explore their effects on the grinding efficiency and hydration process of LS. The results are obtained as the various GAs have optimized the particle size distribution of lithium slag powder, but the changes in specific surface area (SSA) and the relative number of bridging oxygen bonds (RBO) are minor. When the TEA content is 7 g, the leaching rates of Si^{4+} and Al^{3+} from LS powder are the highest, increased by 67.17% and 11.92%, respectively. During the hydration process of the LS-Cement Cementitious Materials

(LCCM), when the dosage of EG is 4 g, it increases the hydration rate of C_2S during the slow reaction stage. Due to the alkaline environment and the distortion of the albite crystal structure, the production of hydration products is increased, the proportion of harmful pores in the hardened paste is reduced, and the strength in the later-age of hydration is improved.

Keywords: Lithium Slag; cementitious materials; grinding aids; triethanolamine; diethylene glycol

0 Introduction

In powder processing technologies of the mining sector, such as mineral processing and beneficiation, the grinding operation is plagued by high energy consumption, rapid equipment wear, and poorly defined limits of particle size reduction. Two primary strategies are employed to enhance grinding efficiency: optimizing the process through equipment upgrades and parameter adjustments, or incorporating grinding aids (GAs) directly into the feed material. However, the wide variety of raw materials leads to differences in physicochemical properties like hardness, chemical composition, and mineralogy. These properties further evolve in complex ways during comminution. As a result, a clear framework for selecting, dosing, and applying GAs remains elusive [1]. In cement production, the most common GAs are alkanolamines [2, 3] and alcohols [4]. This prevalent usage is possibly related to the composition of the cement clinker [5]. During the grinding of clinker minerals, the integrity of the mineral crystalline structure

43 is disrupted. Lattice distortion induces anisotropic charge and enhances the specific
44 surface energy of the ground particles. The particles tend to agglomerate under the
45 influence of van der Waals forces and electrostatic attraction, the particles tend to
46 agglomerate. To mitigate this effect, grinding aid (GA) compounds, which possess high
47 organic polarity, are used to preferentially adsorb onto the exposed broken Ca-O or Si-
48 O bonds on the surface of cement clinker particles [6]. The adsorption reduces polar
49 surface energy and particle adhesiveness, weakens the tendency for agglomeration, and
50 improves the particle size distribution [2]. For instance, Zhou et al. [7] examined the
51 effect of alkanolamine-based GAs on cement clinker grinding. Their results
52 demonstrated that as the growth of the number of methyl groups in the molecular
53 structure of the tertiary alkanolamines, the thickness of the adsorbed molecular layer
54 increases from 9.25 Å to 9.87 Å. While the ability to shield the electrostatic forces
55 between cement particles is enhanced, thereby improving GA performance.
56 The addition of GAs also influences the workability [8–11], mechanical properties [12,
57 13], and durability [14] of cement. For instance, Jiang et al. [15] observed that adding
58 triethanolamine (TEA) to plain cement promoted the formation of AFt during the early
59 stage of hydration, thereby enhancing the compressive strength. However, as hydration
60 progressed, the AFt gradually decomposed, which lowered the later-age compressive
61 strength. In supplementary cementitious materials (SCMs), however, TEA promotes
62 later-age hydration reactions and enhances compressive strength. Consequently, when
63 introduced after clinker grinding, this GA is also referred to an additive [16]. Its primary

function shifts from improving grinding efficiency to participating in the clinker hydration process, analogous to concrete admixtures such as water reducers and accelerators, thereby influencing the performance of cement-based materials. Additionally, gypsum present in cement can modify the effectiveness of TEA [17], which necessitates careful optimization of the proportions among clinker, gypsum, and TEA [18, 19].

Driven by the national policy to "actively and steadily advance carbon peak and carbon neutrality," there has been a growing trend of integrating solid wastes as a supplementary material in cement products. Representative cases include slag powder [20, 21], fly ash [22], and desulfurized gypsum. The chemical composition of these solid wastes differs from that of cement clinker, typically being richer in silica, alumina, or both. In their original state, most possess little to no hydraulic activity. For instance, raw slag exhibits no inherent cementitious properties. Their reactivity can be enhanced through physical and chemical activation. Zepper et al. [21] employed five different GAs to do dry fine milling on basic oxygen furnace slag and found that TEA was also effective for slag powder, not only improving grinding efficiency and reducing particle size but also consequently enhancing its hydraulic activity. Wei et al. [23] investigated the effect of three GAs on the dry fine milling of sugarcane bagasse ash and found that both TEA and a polycarboxylate superplasticizer effectively reduced particle fineness. The improvement in mortar strength was primarily beneficial due to the proportion of fine particles in the 3-32 μm range, which showed the most pronounced increase. Liu

et al. [24] employed TEA and triisopropanolamine (TIPA) as GAs, which effectively increased the SSA of iron tailings powder and suppressed particle agglomeration. The research further revealed that TEA chelated with ions such as $Al^{3+}$and Fe^{3+} in the particles, thereby accelerating the dissolution of aluminum, iron, and calcium ions from the iron tailings powder into the pore solution of the slurry. This process promoted the overall dissolution and enhanced the reactivity of the iron tailings powder. Meanwhile, the hydration heat of the system with TEA is higher than that of systems with TIPA or without GA. In another study, Zhao et al. [25] used chemical-grade glycerol as a GA to improve the grinding efficiency of steel slag and modify its particle characteristics. A notable finding was that the proportion of 3–32 μm particles increased significantly after grinding for 40, 50, and 60 minutes, which is primarily due to the reduction of agglomeration. While a number of studies have investigated the effect of GAs on the hydration reaction engineering of cement-solid waste cementitious systems [8, 20, 21, 26-29], certain conclusions remain inconsistent: in terms of hydration capacity by TIPA and TEA [20, 21]. Hence, it's imperative to further enrich the body of relevant research results.

Although research on using GAs for solid waste utilization is still emerging, the aforementioned studies demonstrate that GAs can enhance the grinding of relevant raw materials, which suggests their potential for adaptation and application in the resource utilization of lithium slag (LS). LS is the waste residue generated from the extraction of lithium salts from lithium ore, rich in silicon and aluminum [30]. LS and fly ash were

both classified both as siliceous-aluminous materials. The utilization of LS in cement products, apart from its direct use as sand in mortar or concrete [31-33], has chiefly focused on applications that require mechanical grinding to enhance its reactivity. These include the production of cement admixtures [34] or all-solid-waste cementitious materials [35-37].

Hence, it is feasible to add GAs during the milling of LS to improve grinding efficiency. This study investigated three types of GAs: alcohols, alkanolamines, and inorganic salts. The effects of GA type and dosage on grinding efficiency and the hydration process of LS were examined using particle size analysis, mechanical property testing, and X-ray diffraction (XRD) to elucidate the underlying mechanisms. Ultimately, this work aims to provide data support for reducing grinding energy consumption and improving the resource utilization of LS, to further refine and expand the theoretical basis of GAs, thereby contributing to clean production and the development of a circular economy in the lithium battery industry.

1 Materials and Methods

1.1 Materials

The chemical compositions of the experimental raw materials are listed in Table 1.

Ordinary Portland cement (OPC). The cement used in the experiment is P·O 42.5 grade OPC. Its density is 3.17 $g \cdot cm^{-3}$, SSA is 374 $m^2 \cdot kg^{-1}$, and 28-day compressive strength is 55.7 MPa.

LS. From Jiangxi Province, China. The density of LS is 2.51 g·cm^{-3}, and the SSA is 264 m^2·kg^{-1}. As shown in Fig. 1(a) by the TG analysis of LS, the evaporative water content is 0.925%, and the non-evaporative water content is 0.754%. The main mineral components of LS are quartz and albite in Fig. 1(b), and the 28-day activity index (R_{28}) is 51.4%. After 30 minutes of grinding LS, the SSA reached 570 m²/kg, and the R_{28} is 92.6%.

GAs. Ethylene glycol(EG, $C_2H_4O_2H_2$), triethanolamine(TEA, $C_6H_{15}NO_3$), and sodium tripolyphosphate(STPP, $Na_5P_3O_{10}$).

Sand. China ISO standard sand.

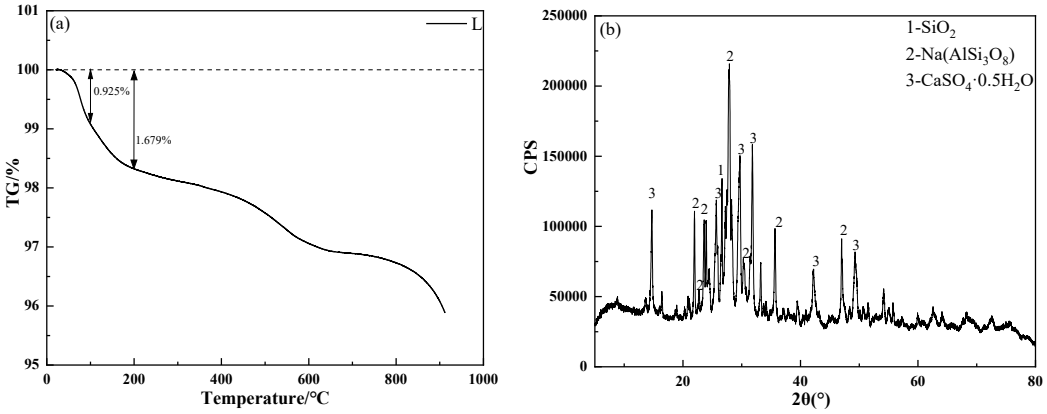


Fig.1 Physical and chemical properties of LS

Table 1 Chemical composition of raw materials (wt. %)

Materials	CaO	SiO_2	Fe_2O_3	MgO	Al_2O_3	TiO_2	Na_2O	K_2O	SO_3	LOI
OPC	56.10	23.26	2.69	3.96	6.89	0.40	0.46	0.67	2.12	3.02
LS	2.89	49.28	0.78	0.25	21.48	3.78	10.21	3.23	0.53	6.71

1.2 Methods

1.2.1 Sample preparation

Put the LS into an electric blast and dry it until the moisture content is less than 0.10%. Weigh 5 kg of LS and mix it respectively with 3 g, 4 g, and 5 g of EG, labeled as LE3, LE4, and LE5; 5 g, 6 g, and 7 g of TEA, labeled as LT5, LT6, and LT7; and 1.5 g, 2.5 g, and 3.5 g of STPP, labeled as LST1.5, LST2.5, and LST3.5. The mixtures are loaded into an SM Φ500 mm × 500 mm cement test ball mill, with a grinding duration of 30 minutes for each group.

1.2.2 Tests procedure

Cement mortar strength test. Refer to Sections 7 and 9 of *"Test method of cement mortar strength (ISO method)"(GB/T 17671-2021)* for the operational procedures.

Activity index test. Refer to the operating method in Appendix B of *"Lithium slag powder for cement and concrete" (YB/T 4230-2010)*.

Preparation of paste samples. Follow the procedure in Section 7 of *"Test methods for water requirement of standard consistency, setting time and soundness of the portland cement"(GB/T 1346-2024)*. After water curing to the specified age, immerse the samples in anhydrous ethanol to stop hydration, and then carry out tests on the hydration mechanism.

Si^{3}+ and Al^{4+} leaching experiment. Take 1 g of ground LS, and simultaneously prepare 100 mL of 1 mol/L NaOH solution to simulate the alkaline environment of cement

hydration. Add the LS to the prepared NaOH solution, stir with a magnetic stirrer at 20°C for 1 hour, then filter the solution through a 0.42 μm filter paper down to 10 mL. Next, dilute the filtered solution with 5% nitric acid to bring the pH below 2. Finally, perform ICP analysis to determine the concentrations of $Si^{3}+$ and Al^{4+}.

1.2.3 Characterization methods

The SSA of raw materials is measured using the QBE-9 fully automatic SSA tester.

The size distributions of the raw materials are tested by a laser particle size analyzer, Mastersizer 2000.

The composition of the raw materials is analyzed by Bruker D8 Advance X-ray diffractometer (Germany), voltage of 40 kV, current of 30 mA, Cu target, 2θ scanning ranging between 10 ° and 80 °, step size of 0.02 °, scanning rate of 5 °·min^{-1}.

TriStar II.302 from Mack Instruments was used to test the concrete hole structure, and the test range was 0.35~500nm.

The X-ray photoelectron spectrometer is measured using the Axis Supra+ instrument with Al Ka radiation to investigate.

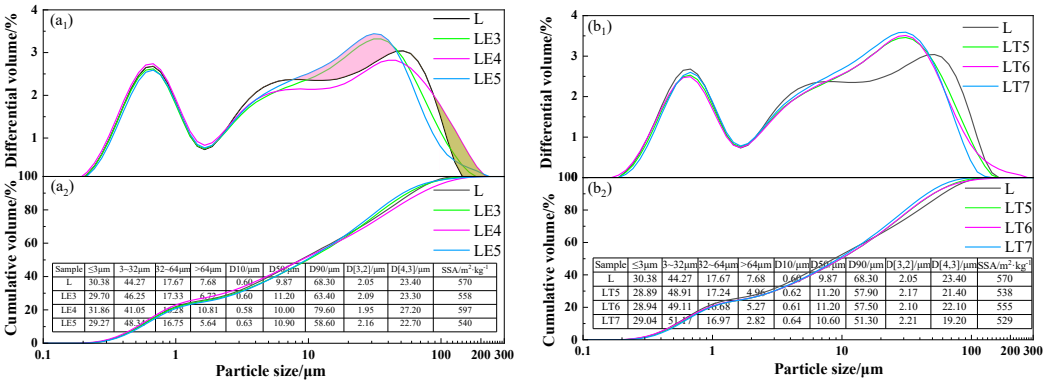
An inductively coupled plasma optical emission spectrometer (ICP-OES) is applied to leach concentrations.

2. Results and Discussion

2.1 Effect of GAs on the Particle Characteristics of LS Powder

2.1.1 Particle Size Distribution of LS Powder

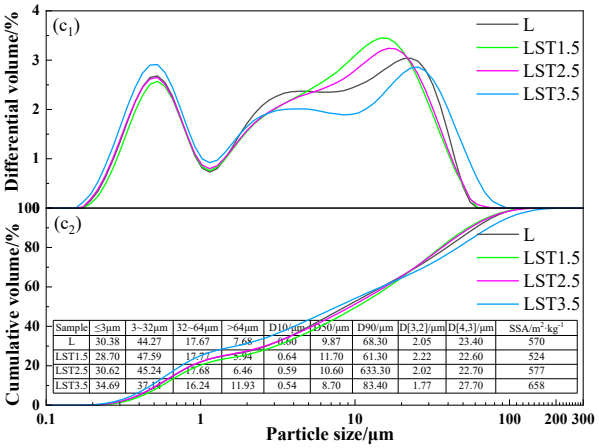
183



Sample	≤3μm	3~32μm	32~64μm	>64μm	D10/μm	D50/μm	D90/μm	D[3,2]/μm	D[4,3]/μm	SSA/m²·kg⁻¹
L	30.38	44.27	17.67	7.68	0.60	9.87	68.30	2.05	23.40	570
LE3	29.70	46.25	17.33	6.72	0.60	11.20	63.40	2.09	23.30	558
LE4	31.86	41.05	16.28	10.81	0.58	10.00	79.60	1.95	27.20	597
LE5	29.27	48.32	16.75	5.64	0.63	10.90	58.60	2.16	22.70	540

Sample	≤3μm	3~32μm	32~64μm	>64μm	D10/μm	D50/μm	D90/μm	D[3,2]/μm	D[4,3]/μm	SSA/m²·kg⁻¹
L	30.38	44.27	17.67	7.68	0.60	9.87	68.30	2.05	23.40	570
LT5	28.89	48.91	17.24	4.96	0.62	11.20	57.90	2.17	21.40	538
LT6	28.94	49.11	16.68	5.27	0.61	11.20	57.50	2.10	22.10	555
LT7	29.04	51.47	16.97	2.82	0.64	10.60	51.30	2.21	19.20	529

184



Sample	≤3μm	3~32μm	32~64μm	>64μm	D10/μm	D50/μm	D90/μm	D[3,2]/μm	D[4,3]/μm	SSA/m²·kg⁻¹
L	30.38	44.27	17.67	7.68	0.60	9.87	68.30	2.05	23.40	570
LST1.5	28.70	47.59	17.77	5.94	0.64	11.70	61.30	2.22	22.60	524
LST2.5	30.62	45.24	17.68	6.46	0.59	10.60	633.30	2.02	22.70	577
LST3.5	34.69	37.64	16.24	11.93	0.54	8.70	83.40	1.77	27.70	658

185 **Fig.2** Effect of GAs on the particle size distribution of LS powder

186 Note: D[3,2] is average particle size by surface area, D[4,3] is average particle size by volume.

187 The present research intended to assess the effects of GAs on the milling performance
188 of LS, with initial attention directed toward particle size outcomes. Figure 2 compares
189 the particle size distributions of LS powder processed with different types and dosages
190 of GAs. The particle size distribution of Group L was trimodal, with peaks at
191 approximately 0.1–2 μm, 2–8 μm, and 30–80 μm. This indicates relatively poor
192 uniformity and continuity in particle size distribution. In contrast, the introduction of
193 TEA exhibited a bimodal pattern. The distributions produced by the samples of LE and
194 LS corresponded to the two patterns mentioned above, an outcome attributable to the

differences in dosages. Overall, with respect to particle uniformity and continuity, TEA demonstrated a relatively stable effect on LS powder.

Based on the particle size data derived from Figure 2, the proportion of particles below 7 μm increased in Group LE4, whereas the maximum particle size was also elevated from 144 μm to 272 μm. In sample LT, it reduced the proportion of particles smaller than 119 μm, while the maximum particle size rose from 144 μm to 240 μm, and the proportion of particles in the 3-32 μm range increased. The particle size distribution exhibited noticeable changes with higher dosages of STPP. Notably, Group LST3.5 not only broadened the overall size range but also enhanced the proportion of fine particles. Overall, the three GAs produced limited changes in the minimum particle size, the proportion of each particle size range, and the SSA of the LS powder. However, the maximum particle size was generally elevated. This might be attributed to a reduction in inter-particle adhesion force induced by the GAs [2], thereby likely lowering the probability of contact between large particles and the grinding media. Hence, from the perspective of particle size distribution, the physical influence of these three GAs on LS powder was not pronounced.

2.1.2 FT-IR Analysis of LS

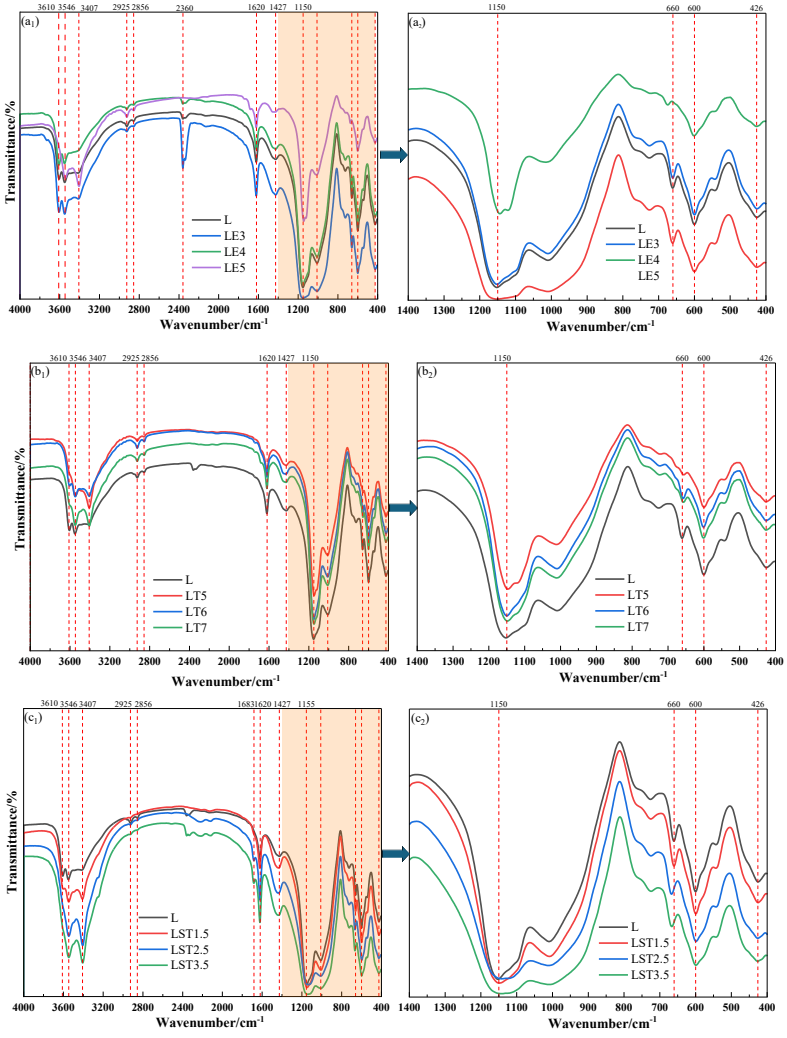
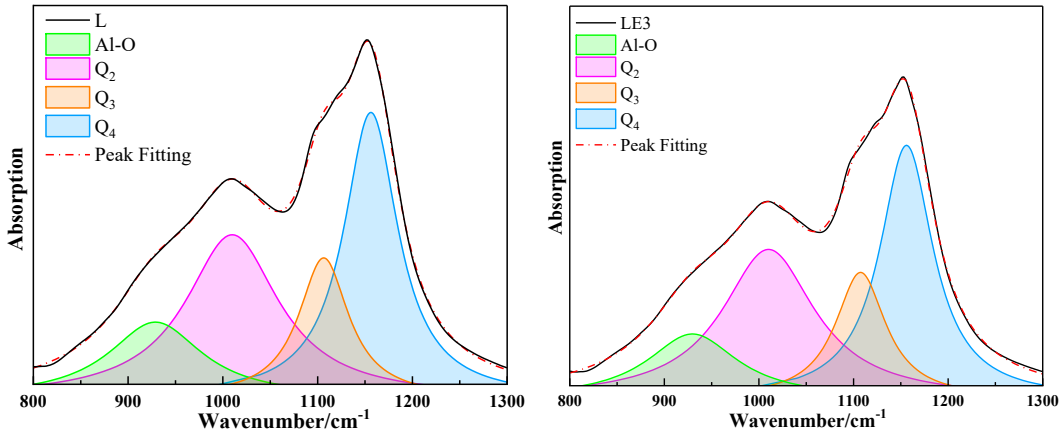
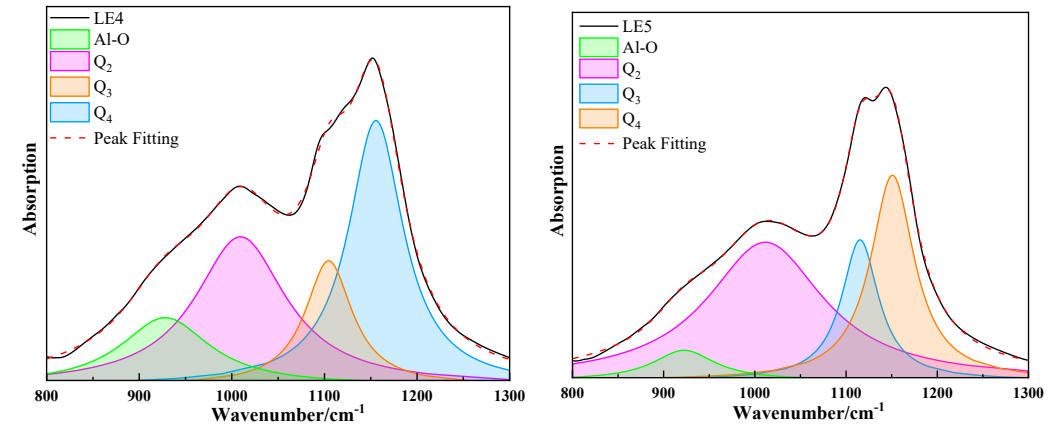


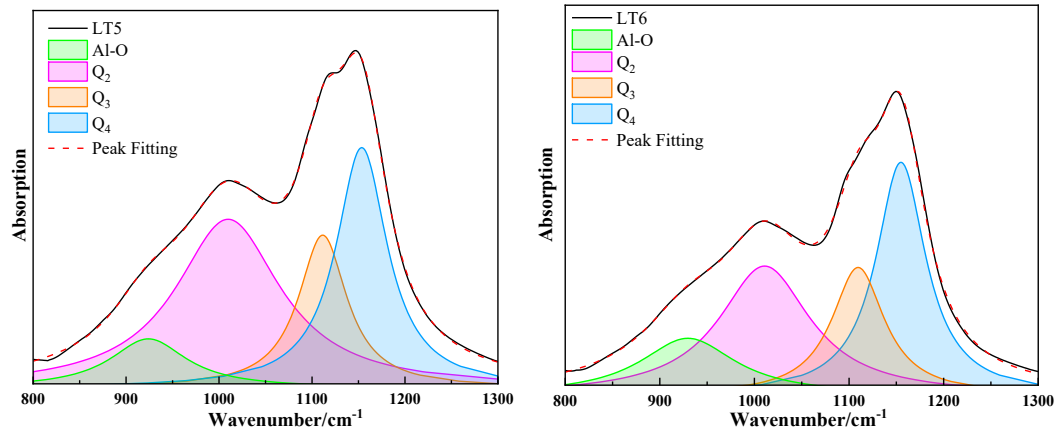
Fig. 3 Test of FT-IR



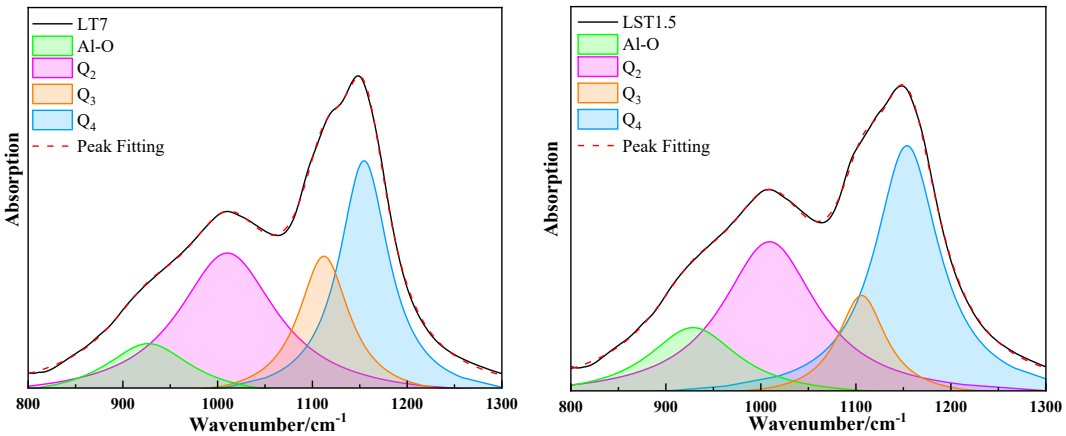
218



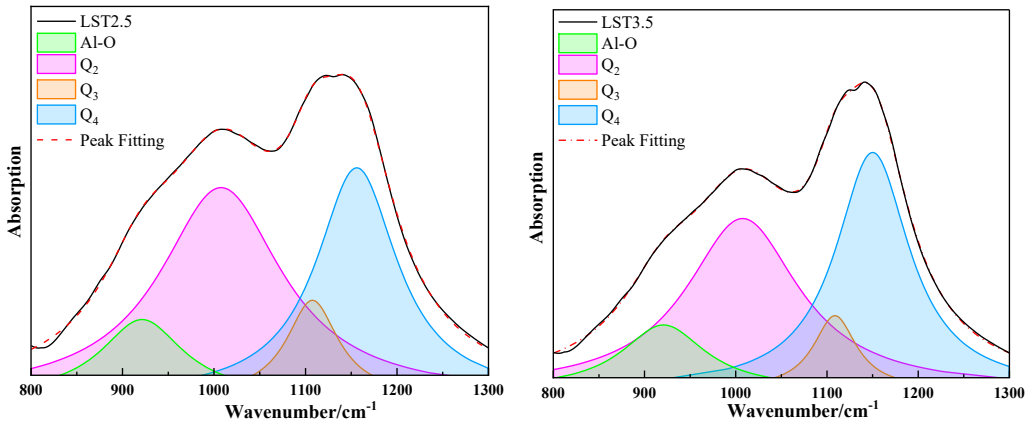
219



220



221



222

223 **Fig. 4** Area Fitting

224 To clarify the influence of GAs on the molecular and crystalline structure of LS, Fourier

225 Transform Infrared (FT-IR) spectroscopy was conducted, with the results displayed in

226 Figure 3.

227 In Group L, the absorption band at 3610 cm^{-1} is likely attributed to the asymmetric

228 stretching vibration of O-H in non-evaporable water in the slag. The band at 3546 cm^{-1}

229 may correspond to the hydrogen-bonded O-H stretching vibration within β-

230 $CaSO_4 \cdot ½H_2O$, while the band at 3407 cm^{-1} is likely associated with the H-O-H

231 stretching vibration in $CaSO_4 \cdot 2H_2O$. Notably, the absorption peak at 3610 cm^{-1}

232 gradually diminished with increasing dosages of TEA and STPP in Figure 3 (b_1) and

233 Figure 3 (c_1), possibly due to their acceleration of non-evaporable water loss.

234 The bands at 2925 cm^{-1} and 2850 cm^{-1} correspond to the asymmetric and symmetric

235 respectively stretching vibrations of $–CH_2–$. The absorption peak at 2360 cm^{-1} is

236 characteristic of O=C=O stretching, while that at 1620 cm^{-1} is assigned to –C=C–

237 stretching. The band around 1427 cm^{-1} arises from the symmetric stretching of the C–

238 O bond. These signals likely originate from organic compounds or carbonates
239 introduced during the preparation of LS.
240 The spectral region relevant to the hydration capacity of LS lies mainly between 1300
241 and 400 cm^{-1}, encompassing vibrations of siloxane and aluminoxane groups. Within
242 this range, the band at 1200–1100 cm^{-1} corresponds to the symmetric stretching
243 vibration of SO_4^{2-}, while the region between 1200 and 800 cm^{-1} is attributed to the
244 symmetric stretching vibration of Si–O bonds, which reflects the number of bridging
245 oxygens (Q^1, Q^2, Q^3, Q^4) in silicon-oxygen tetrahedra. The band near 660 cm^{-1} is
246 assigned to the bending vibration of Si–O–Si, and the band around 600 cm^{-1}
247 corresponds to the deformation vibration of Si–O–Al. At approximately 426 cm^{-1}, the
248 in-plane and out-of-plane bending vibrations of Si–O are observed.
249 In Figure 3 (a_2)， the increasing dosage of EG progressively altered the absorption peak
250 in the 1200–1100 cm^{-1} range, causing its shape to shift from sharp to blunt, and then
251 back to sharp. This indicates that EG influenced the symmetry of the S–O stretching
252 vibration in SO_4^{2-}, possibly leading to multiple vibrational modes. The peak position
253 was observed to shift first to higher and then to lower wavenumbers. Additionally,
254 Group LE5 exhibited higher transmittance at the 660 cm^{-1} band, indicating partial
255 decomposition of some Si–O–Si bonds.
256 In Figure 3 (b_2), the dosage of TEA also influenced the symmetry of the S–O bond
257 stretching vibration in SO_4^{2-}. As the content of TEA increased, the shape of the
258 absorption peak at 660 cm^{-1} transitioned from sharp to blunt and then gradually

sharpened again, indicating that TEA affected the symmetry of the Si–O–Si stretching vibration. Concurrently, the gradual shift of this peak to lower wavenumbers suggests a weakening of the Si–O–Si bond strength. The shape of the absorption peak at 600 cm^{-1} also sharpened accordingly, further indicating that TEA promoted the symmetry of the Si–O–Al deformation vibration.

In Figure 3 (c_2), STPP weakened the symmetry of the S–O stretching vibration in SO_4^{2-} and likely resulted in multiple vibrational modes, while also lowering the bond energy of the S–O bond. With increasing STPP dosage, the absorption peak at 660 cm^{-1} gradually changed to higher wavenumbers, suggesting an enhancement of Si–O bond strength. Simultaneously, the sharpening of the peak at 600 cm^{-1} indicates that STPP weakened the symmetry of the Si–O–Al deformation vibration.

The degree of polymerization of silicon-oxygen tetrahedra and the relative area of the Al–O bond are fitted using the Lorentz function, with the results shown in Figure 4. Following the method of Zhang et al. [38], the Relative Bridging Oxygen number (RBO) is calculated to reflect the relative extent of polymerization or depolymerization, with the results summarized in Table 2. Figure 4 shows that the Q^1 species does not appear in the fitting due to its low content rather than its complete absence. As in Table 2, the proportion of Q^2 increased with the dosage of most GAs. The proportion of Q^3 rose with the dosage of EG and TEA but exhibited an opposite trend with STPP. The proportion of Q^4 remained largely unchanged. The RBO value increased only slightly in the Group LE3, Group LE4, and Group LST1.5. Conversely, the relative area of the Al–O bond

generally decreased with increasing dosage of most GAs. Thus, the incorporation of an appropriate amount of GA favorably modified the structure of LS by decreasing the polymerization degree of its silicon-oxygen tetrahedra. The resultant increase in Q^2 and Q^3 species enhanced the hydration potential of Si–O bonds, and the hydration capacity of Al–O bonds was improved as a combined effect.

Table 2 Area ratio and RBO/%

Sample	Q^2	Q^3	Q^4	Al-O	RBO
L	33.1	16.5	35.6	14.8	75.7
LE3	29.3	17.8	36.6	16.3	77.2
LE4	33.0	15.6	37.2	14.2	76.2
LE5	46.8	17.6	29.7	5.8	70.4
LT5	41.0	19.1	31.1	8.8	72.3
LT6	32.3	19.8	33.8	14.2	75.5
LT7	36.1	19.9	32.2	11.8	73.9
LST1.5	34.4	12.5	38.9	14.2	76.3
LST2.5	44.6	9.9	34.1	11.4	72.0
LST3.5	41.2	7.8	39.5	11.6	74.6

2.1.3 Dissolution Rates of Silicon and Aluminum Ions (Si^{4+} and Al^{3+}) from LS

The dissolution rates of silicon and aluminum ions from LS are determined by inductively coupled plasma optical emission spectrometry (ICP-OES, PerkinElmer

290 Optima 8300). Mechanical grinding disrupts the crystalline and amorphous structures
291 within the LS, liberating hydration-active components. Therefore, ICP-OES testing of
292 Si and Al dissolution rates serves as a method for evaluating the reactivity of pozzolanic
293 raw materials. The corresponding data are summarized in Table 3. The results reveal
294 that the dissolution rate of Al^{3+} consistently exceeded that of Si^{4+}. According to bond
295 length calculations for albite crystals reported by Wang et al. [39], the bond lengths
296 follow the order Si–O < Al–O < Na–O. Given that longer bond lengths generally
297 correspond to weaker bond energies, the Si-O bond therefore had a higher bond energy
298 than the Al-O bond and required more energy to break the bond. The addition of EG
299 and TEA to LS both increased the leaching rates of Si^{4+} and Al^{3+}, although the
300 enhancement was not pronounced. However, STPP only increased the leaching rate of
301 Si^{4+} while inhibiting that of Al^{3+}, a result consistent with the analysis presented in Table
302 3.
303 In conclusion, based on the collective assessment of the physical and chemical impacts
304 of the three GAs on LS, it is preliminarily concluded that the GAs do not significantly
305 enhance the hydration ability of LS.
306
307 **Table 3** Leaching rate/%

Sample	Si^{4+}	Al^{3+}
L	0.1453	8.5148
LE3	0.1486	8.4926

LE4	0.1535	8.7444
LE5	0.1562	8.8275
LT5	0.1855	8.8732
LT6	0.2167	9.3572
LT7	0.2429	9.5298
LST1.5	0.1583	8.3719
LST2.5	0.1784	8.2652
LST3.5	0.1879	7.9325

2.2 Effect of GAs on the Hydration Process of LCCM

2.2.1 Hydration Activity

The activity index scheme for LS and the results are listed in Table 4.

As shown in Table 4, Group LC demonstrated a 3-day compressive activity index of 69.7% and a 28-day index of 92.6%. Both values fell below the standard thresholds of 70% and 95%. Therefore, to improve the activity index, it is necessary to further investigate the influence of GAs on the hydration activity of LS.

Results of the other groups show that the addition of GAs led to varied mechanical performance in LS-incorporated LCCM. In terms of compressive strength, EG depressed the early-age activity index, maintained the mid-term index, and enhanced the later-age index. This is evidenced by Group LE4C, which reached a 28-day activity index of 106.1%. Both TEA and STPP reduced the early- and mid-term activity indices

but enhanced the later-age performance, as evidenced by Groups LT6C and LST2.5C. Critically, the strength development of cementitious materials is governed by a combination of hydration activity, particle size distribution, and the pore structure of the hardened matrix.

Table 4: Mix ratio and Strength at different curing ages

Sample	Cement/g	LS/g	Water/g	Sand/g	FS of 3d/MPa	CS of 3d/MPa	FS of 28d/MPa	FS of 3d/MPa
C	450	0	225	1350	5.4	35.6	8.1	55.7
LC	315	135			4.0	24.8	7.3	51.6
LE3C					3.8	23.0	6.7	56.5
LE4C					4.4	24.2	7.3	59.1
LE5C					4.3	22.3	6.7	52.2
LT5C					3.6	20.9	6.1	49.5
LT6C					3.9	23.8	6.8	55.1
LT7C					3.1	21.9	7.6	53.4
LST1.5C					3.7	21.9	7.5	52.2
LST2.5C					3.8	21.7	7.3	53.6
LST3.5C					3.2	23.6	9.6	50.8

Note: FS is flexural strength, CS is compressive strength

2.2.2 Heat of Hydration of the LCCM

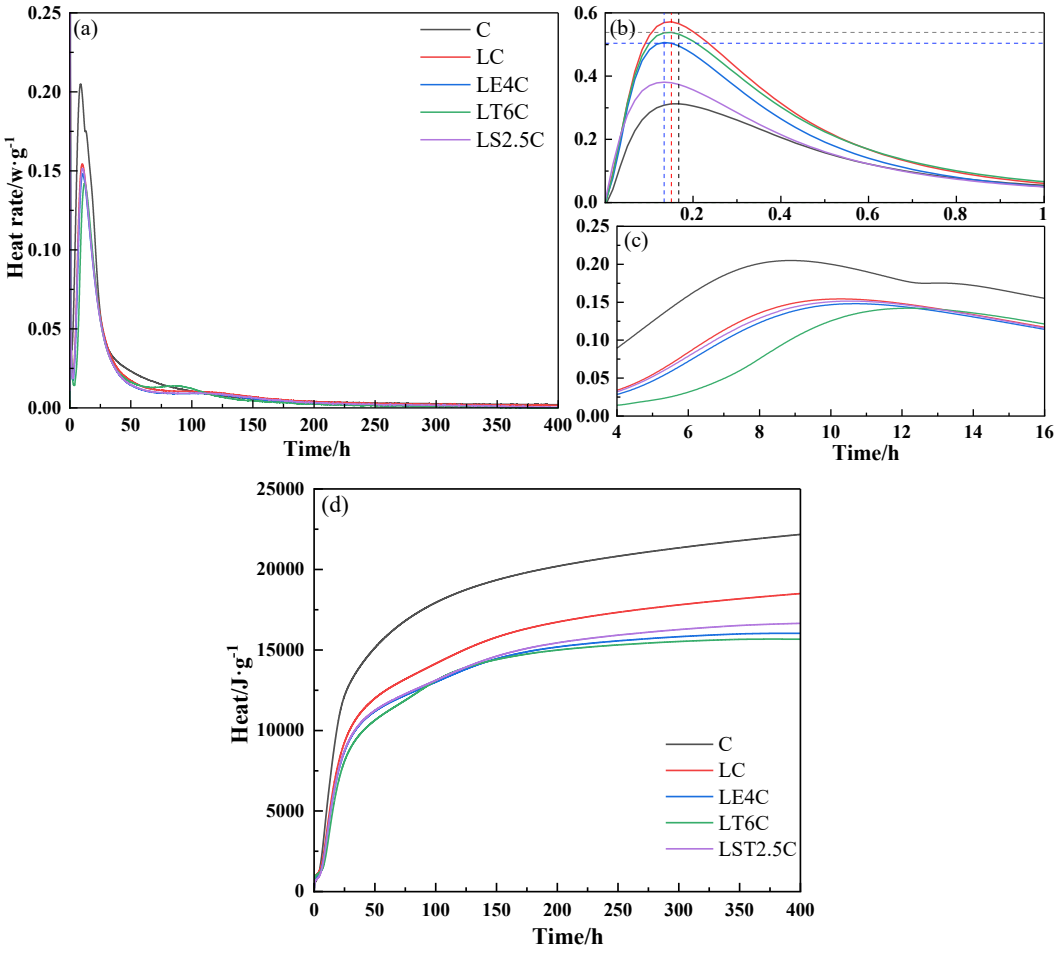


Fig. 5 Release heat

The hydration heat release rate curves for all cementitious materials systems are presented in Figure 5 (a). The overall progression of the hydration reaction is similar across all groups, indicating that neither the incorporation of LS nor the GAs altered the five characteristic stages of cement hydration. The initial period, typically within the first 15 minutes, is dominated by heat release from the dissolution of cement phases, the reaction of C_3A and C_4AF with gypsum to form AFt, along with the early hydration of C_3S, with the early hydration of C_3S contributing a relatively small amount of heat at this stage. And in Figure 5 (b), both the rate and the magnitude of the first exothermic

peak are higher for LCCM than for pure cement (dashed line). This is primarily because the hydration activity of LS in LCCM can be considered negligible at this early stage, and the reduced cement content effectively increases the water-to-binder ratio. According to the "delayed dissolution theory," this results in an undersaturated liquid phase, which accelerates the dissolution of cement [40].

In contrast, the first exothermic peak is lower in all GAs-containing groups compared to Group LC. Among them, Group LE4C and Group LST2.5C reached their peak rates earlier and almost simultaneously, followed by Group LT6C and Group LC, which peaked at a similar later time. Particle size analysis in Figure 2 shows that for particles below 20 μm, Group LC had the highest content, followed by Group LST2.5C. For particles above 20 μm, this order was reversed. However, Group LST2.5C exhibited the lowest heat release rate among the GA-containing groups. This suggests that despite the higher fine particle content, STPP inhibited the early hydration of C_3A and C_4AF. Groups LE4C and LT6C also exhibited lower heat release rates than Group LC. While Lu et al. [41] reported that TEA accelerates the hydration of C_3A and C_4AF, the observed effect here is likely the combined result of particle size distribution and modified hydration kinetics.

The acceleration period is governed primarily by the hydration of C_3S and C_2S. Figure 5 (c) shows that pure cement exhibited a higher heat release rate than LCCM, as a result of its higher C_3S content. The composite materials not only displayed lower peak rates but also delayed peak times, indicating that the GAs generally retarded the hydration of

362 both C_3S and C_2S. This retardation effect is most pronounced in Group LT6C. As for

363 the stable period, it is mainly associated with C_2S hydration. As seen in Figure 5 (d),

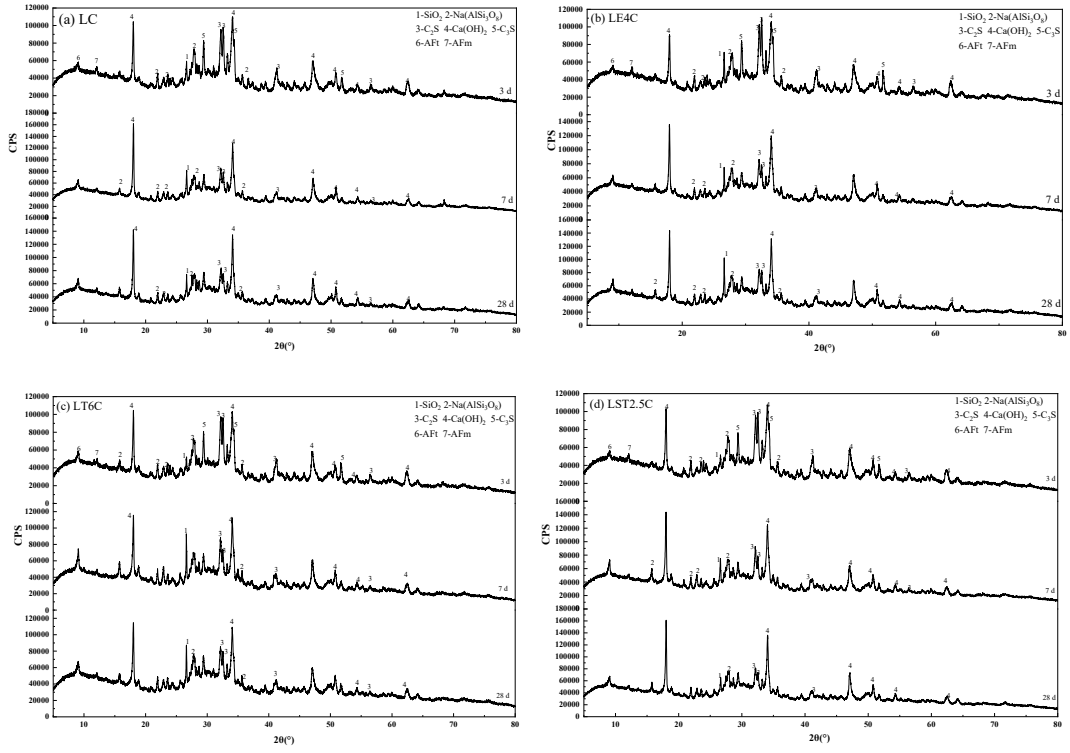
364 Group LST2.5C shows that STPP appeared to enhance C_2S hydration under these

365 conditions, whereas Group LE4C and Group LT6C exhibited an inhibitory effect.

366

367 2.2.3 XRD Analysis of the LCCM

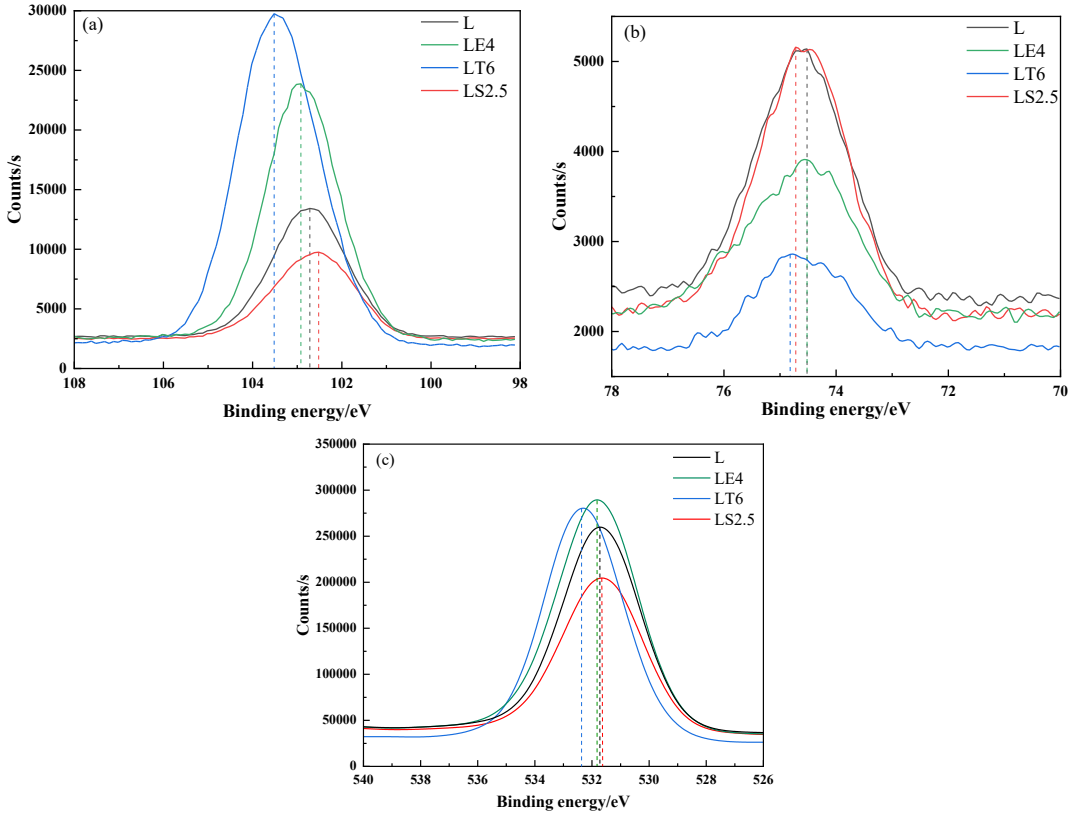
368



369

370 **Fig.6** XRD patterns of the hydration products

371



372

373

374 **Fig. 7** XPS of LS (a)Si, (b)Al, (c)O

375

376 Since the hydration products of pure cement, which typically include crystals such as
377 AFt, AFm, and SiO_2, are well established, XRD analysis is not separately performed
378 for Group C. Figure 6 presents the hydration products' XRD patterns of for the LCCM,
379 in which the addition of GAs do not lead to the formation of new mineral phases.
380 Figure 6 (a) shows that the incorporation of LS into cement resulted in the presence of
381 albite among the hydration products. With increasing curing age, the intensity of the
382 main albite peak located at 27°–28°, which corresponds to the (040) plane, gradually
383 decreased. Meanwhile, the intensity of the albite peak at 15~16°, associated with the
384 (111) plane, increased. This suggests partial decomposition and polycrystallization of
385 albite within the alkaline environment. Moreover, in Group LE4C, alongside these

386 changes in albite, the intensity of the quartz peak gradually increased. In contrast, in
387 Groups LT6C and LS2.5C, the quartz peaks first increased and then decreased. This
388 implies that the addition of GAs may have affected the hydration of C_3S, C_2S, or albite
389 during the hydration reactions of cementitious materials.
390 Further comparison of the XRD patterns of each experimental group shows that after
391 adding GAs, the C_3S peak intensity is slightly lower than that in Group LC, indicating
392 that GAs slightly promoted the hydration of C_3S. However, adding C_2S and $Ca(OH)_2$
393 behaved differently. A compression of C_2S and $Ca(OH)_2$ between the Group LC and
394 Group LE4C reveals that the $Ca(OH)_2$ peaks (17~18°, 33~34°) in Group LE4C are
395 lower than those in Group LC at each curing ages, whereas the C_2S peaks (31~33°,
396 33~34°, 40~42°) in Group LE4C are higher than those in Group LC at each curing ages,
397 suggesting that EG inhibited the hydration of C_2S in curing period. Group LT6C shown
398 the same trend. Group LS2.5C is slightly different: STPP only promotes the hydration
399 of C_2S at 28 days, confirming the conclusion about the stability period in Section 2.2.2.
400 Consequently, the gradual increased in the quartz peak is largely related to the GA-
401 promoted hydration reaction of albite. Thus, to verify this, XPS analysis is performed
402 and shown in Figure 7.
403 According to the XPS database, the binding energy of Si2p in albite is approximately
404 102.80 eV, while such energy in SiO_2 crystals is about 103.50 eV. As shown in Figure
405 7 (a), the measured binding energy of Si2p in Group L is around 102.70 eV, slightly
406 lower than the database reference, which may reflect structural variations of the albite

407 within LS. Groups LE4 and LT6 showed elevated Si2p binding energies higher than
408 those in Group L. This increase suggests electrons loss from Si2p, an increase in Si–O
409 bond energy, and a progression from the aluminosilicate chemical state toward the SiO_2
410 crystal state. In contrast, Group LST2.5 gained electrons and reduced the Si-O bond
411 energy. Based on the XPS database reference, the binding energy of Al2p in albite is
412 approximately 74.70 eV. Figure 7 (b) shows the value in Group L to be around 74.60
413 eV., closely matching the reference. It's indicated that Si2p in Group LE4 and Group
414 LT6 loss electrons, enhanced the Si-O bond energy and shifted from the aluminosilicate
415 chemical state toward the SiO_2 crystal. In contrast, Group LS2.5 gained electrons and
416 reduced the Si-O bond energy.
417 The binding energies for Groups L, LE4, and LST2.5 are similar, while Group LT6
418 exhibited a slight shift to a lower value, suggesting a potential increase in Al-O bond
419 energy. Reference O1s binding energies are about 531.10 eV in Al_2O_3 and 532.90 eV in
420 SiO_2. Figure 7(c) indicated that the O1s binding energy in Group L is closer to the
421 alumino-oxygen state. All GA-contained groups shifted towards the silico-oxygen state,
422 with Group LT6 showing the most significant change, suggesting electron loss from the
423 alumino-oxygen state induced by the GAs.
424 Based on this, the chemical mechanism of GAs on LS can be summarized. EG and TEA
425 increased the binding energies of Si2p and O1s in albite, thereby enhancing Si-O bond
426 energy and promoting the stability of silicon-oxygen tetrahedra. While the increase or
427 constancy in the Al2p binding energy, combined with the rise in O1s binding energy,

led to a reduction in the symmetry of the aluminoxane tetrahedral structure. STTP decreased the binding energies of Si2p and O1s, therefore reducing Si-O bond energy and destabilizing silicon-oxygen tetrahedra, while its effect on Al2p and O1s promoted the stability of alumino-oxygen tetrahedra. This explains the decreased Al^{3+} dissolution rate and the opposite trend for Si^{4+} with increasing STPP dosage (Table 3).

Therefore, within the LCCM, the chemical role of the GAs is to destabilize the albite crystal structure and modify the alkaline environment provided by cement hydration, collectively accelerating albite hydration.

2.2.4 Thermogravimetric Analysis (TG-DTG) of the LCCM

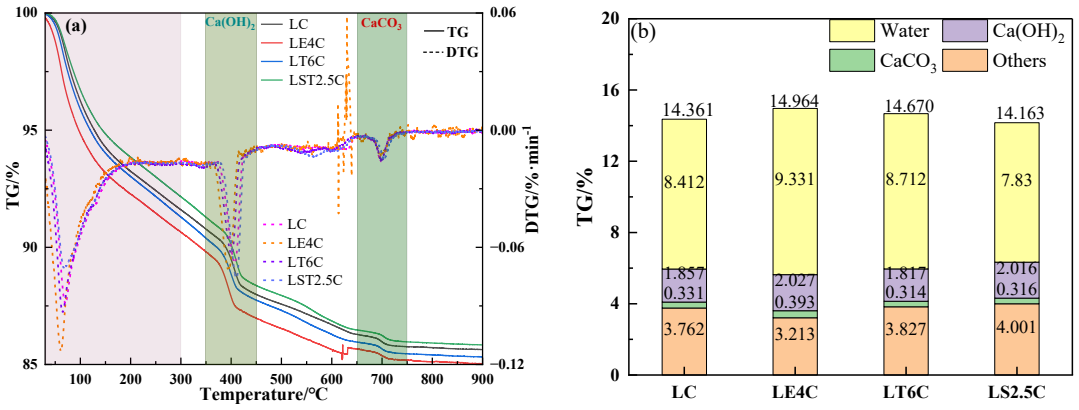


Fig. 8 TG-DTG

Figure 8 presents the thermal analysis of the hydration phases for each group after 28 days of curing. The dehydration of free and bound water in phases such as C-S-H and AFt occurs between room temperature and 300°C. As shown by the derivative thermogravimetry (DTG) curves in Figure 8 (a), the corresponding peaks within this temperature range appear as singlets without shoulders, indicating a low content of the

AFm phase. A notably sharp DTG peak was also observed in this region, which corresponded to the highest weight loss rate (9.331%) in Figure 8 (b), suggesting a relatively higher AFm phase content. Hence, the enhanced mechanical performance resulting from these hydration products further explicates the superior 28-day compressive strength of Group LE4C recorded in Table 4. The decomposition of $Ca(OH)_2$ takes place between 350°C and 550°C, with the associated DTG absorption peak appearing near 400°C. Figure 8 (b) also shows that Group LE4C has the greatest weight loss attributed to $Ca(OH)_2$ decomposition, which indicates a higher portlandite content and, consequently, a higher pH within the hardened paste, thereby supporting and extending the conclusions drawn in Sections 2.2.2 and 2.2.3. The minor thermal event observed around 630°C for Group LE4C is ascribed to the release of occluded water and does not influence the interpretation of the primary results.

2.2.5 Pore Structure of the LCCM

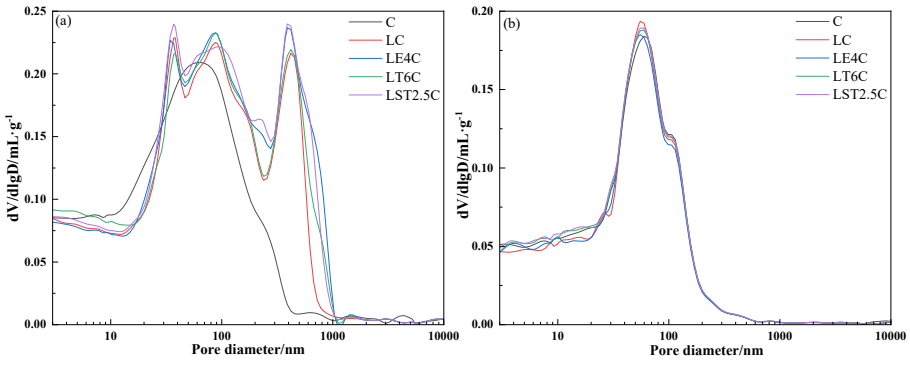


Fig. 9 Differential pore size distribution at different curing ages (a) 3d, (b)28d

Porosity reflects the compactness of hardened paste. Lower porosity indicates fewer pores, more complete solid filling, and higher compactness. Pores are classified by Wu

463 [42] as harmless (<20 nm), less harmful (20–50 nm), harmful (50–200 nm), and more
464 harmful (>200 nm). C-S-H gel pores (0.5–2.5 nm) are below the equipment's detection
465 limit (>3 nm) and thus not considered.
466 Pore structure data are recorded in Tables 5 and 6. Table 5 demonstrates that the porosity
467 of harmless pores (<20 nm) in Group C was higher than in Group LC but lower than in
468 other groups. This trend is likely caused by the combined physical and chemical effects
469 of LS on the cementitious material. Adding LS increased the content of particles smaller
470 than 1 μm, thereby improving the packing density within this size range. As shown in
471 Figure 5 (b), it exhibited a higher early hydration rate. Thus, Group LC is more effective
472 than Group C in reducing the proportion of small pores. In contrast, the higher
473 proportion of pores smaller than 20 nm in Groups LE4C, LT6C, and LST2.5C compared
474 to Group LC is primarily due to chemical effects. Specifically, the retardation of cement
475 hydration by the GAs, as also indicated in Figure 5 (b), resulted in a relatively higher
476 residual water content within the pores.
477 The porosity for pores >20 nm and the total porosity in Group C are both lower than in
478 other groups (Table 5). Since less harmful pores have a relatively minor influence on
479 strength, the following analysis focuses on the contribution of harmful and more
480 harmful pores. When water is added to the cementitious materials, larger particles are
481 surrounded by more adsorbed water compared to finer ones. Moreover, during the early
482 stages of hydration, these coarse particles undergo minimal reaction. Therefore, the
483 larger the particle, the greater the probability that larger pores will form around it.

Figure 6 is the differential pore size distribution curves for each experimental group (the maximum value on the Y-axis represents the most probable pore size). According to Figure 9 (a), the most frequent pore size in Group C ranged between 55 nm and 70 nm, while the other groups exhibited three distinct pore size ranges, with the largest one approximately between 400 and 500 nm. Hence, the inferior 3-day strength of the LCCM, relative to pure cement, can be explained from a pore structure standpoint by the abundance of large, inert particles in the slag, which increases the porosity of harmful and larger pores.

With prolonged curing, the continuous formation of hydration products enhanced the compactness of the paste and refined its pore structure. This improvement is reflected in Table 6, where all porosity parameters are lower than their corresponding values in Table 5. Furthermore, as shown in Figure 9 (b), the most frequent pore sizes for all groups converged toward a similar, narrower range.

Therefore, analysis of the pore structure indicates that incorporating GAs into the composite cementitious material increased the early-age porosity and resulted in a more complex pore size distribution. Meanwhile, their negative impact on the pore structure is less pronounced at later ages.

Table 5 Porosity of different pore sizes after 3 days of curing age/%

Sample	0-20 nm	20-50 nm	50-200 nm	> 200nm	Total porosity	> 50nm

C	11.03	15.71	6.23	3.33	36.30	26.34
LC	10.35	17.15	9.53	3.78	40.81	32.61
LE4C	11.47	17.79	10.17	4.59	44.02	33.53
LT6C	11.16	17.63	9.74	3.98	42.51	32.27
LST2.5C	11.32	18.24	12.38	4.02	45.96	35.68

503

504 **Table 6** Porosity of different pore sizes after 28 days of curing age/%

Sample	0-20 nm	20-50 nm	50-200 nm	> 200nm	Total porosity	> 50nm
C	9.84	12.01	5.44	2.28	29.57	26.11
LC	9.26	12.84	7.33	2.32	31.75	30.39
LE4C	10.48	12.97	7.02	1.01	31.48	25.51
LT6C	10.74	12.86	7.37	2.55	33.52	29.59
LST2.5C	10.86	13.18	8.03	3.21	35.28	31.86

505

506 **3. Conclusions**

507 This study investigated the effects of GAs on LS activity and on the hydration of LCCM.

508 The main conclusions are:

509 (1) Impact of GAs on the particle size distribution of LS. Adding GAs during LS

510 grinding has a limited effect on the minimum particle size but modifies the distribution

511 by increasing the fraction in the 3–32 μm range. It also increased the maximum particle

size by 188.89% for Group LE4, 166.67% for Group LT6, and 129.67% for Group LST3.5，while SSA changes are within 10%. The grinding effect on LS thus differed from their typical performance in cement systems: increased grinding efficiency, narrowed particle size distribution, and enlarged the SSA.

(2) Chemical effects of GAs on LS. The addition of an appropriate dosage of GAs increase the binding energies of Si2p, Al2p, and O1s in LS. It resulted in a higher Si–O bond energy and reduced the symmetry of the aluminoxane tetrahedral structure, thereby destabilizing the albite crystals. Consequently, the degree of polymerization of the silicon-oxygen tetrahedra decreased from 75.7% to 70.4%. These changes promoted the dissolution rates of both silicon and aluminum ions and enhanced the hydration capacity of the slag, although the reduction in crystalline content remained limited.

(3) Effects of GAs on the hydration process of LCCM. The observed reduction in early age strength and the increase in later age strength for Group LE4C can be attributed to the dual role of EG during hydration. During the acceleration period of hydration, EG inhibited the hydration of both C_3S and C_2S, whereas it accelerated the hydration of C_2S during the subsequent stable period. At later curing ages, the increased $Ca(OH)_2$ content, along with the distortion of the albite crystal structure in the LS, jointly promoted the formation of hydration products. These products filled the pores in the hardened paste, which improved its compactness and ultimate strength.

Declarations

Ethics approval and consent to participate

Not applicable.

Consent for publication

Not applicable.

Availability of data and materials

The raw data supporting the conclusions of this article will be made available by the authors, without undue reservation.

Competing interest

The authors declare that they have no conflicts of interest.

Funding sources

The authors gratefully acknowledge financial support by the Key Research and Development Program of Xinjiang Uygur Autonomous Region (2024B04042); the State Key Laboratory of Solid Waste Reuse for Building Materials (SWR-2023-007); State Environmental Protection Key Laboratory of Mineral Metallurgical Resources Utilization and Pollution control (HB2023060); Open Foundation of Hebei Province Key Laboratory for Low-Carbon Construction and Resilience Enhancement of Construction Engineering (HKL-LRC-2024-2, HKL-LRC-2025-8); Funded by Science Research Project of Hebei Education Department (BJ2026058).

Authors' contributions

Kaifan ZHANG propose method and writes manuscript; Xiaojun WANG and Changlong WANG propose and participates in design research and reviews paper; Tianyong HUANG and Yunyi BAI

participate in design research and reviews paper. All the authors approved the final version of the manuscript.

Acknowledgement

The author expresses gratitude to all personnel associated with the various funding sources. We also extend our appreciation to the Beijing Building Materials Academy of Sciences Research for providing equipment support.

References

[1] Ding Yarong, Yang Congren, Fan Jiazhi, Wang Xu, Ma Kunlin, Dong Rongzhen, Bai Pengfei, Zhan Qixian. Research progress on effect of GAs on grinding and application [J]. Journal of Central South University (Science and Technology), 2024, 55(11): 4030-4042.

[2] Dong Yaowu，Sun Zhenping, Zhou Xiaoyang，Yang Sheng, Setzer Max Josef. Effect of Triethanolamine and Sodium Tripolyphosphate as GAs on the Surface Properties of Cement Particle [J]. Journal of building materials, 2022, 25(07): 722-729.

[3] Yinwen Li, Huayu Zhu, Chaolong Yang, Yunfei Zhang, Jing Xu, Mangeng Lu. Synthesis and super retarding performance in cement production of diethanolamine modified lignin surfactant [J]. Construction and Building Materials, 2014, 52: 116-121.

[4] Franco Zunino, Karen Scrivener. Assessing the effect of alkanolamine GAs in limestone calcined clay cements hydration [J]. Construction and Building Materials, 2021, 266: 121293.

574 [5] Eric Nthiga Njiru, Jackson Wachira Muthengia, Onesmus Mulwa Munyao, Daniel
575 Karanja Mutitu, David Munyao Musyoki. Review of the Effect of GAs and Admixtures
576 on the Performance of Cements [J]. Advances in Civil Engineering, 2023, 1: 6697842.
577 [6] Joseph J. Assaad, Camille A. Issa. Effect of clinker GAs on flow of cement-based
578 materials [J]. Cement and Concrete Research, 2014, 63:1-11,
579 [7] Yongfang Zhou, Jianfeng Wan, Yan Song, Hui Liu. Study on structure-performance
580 relationship and action mechanism of organic chemicals in cement Gas [J]. Materials
581 Letters, 2024, 364: 136365.
582 [8] Yahya Kaya, Veysel Kobya, Yunus Kaya, Ali Mardani. Impact of PCE-based GAs
583 on hydration kinetics in fly ash substituted systems: Influence of pH and dosage [J].
584 Construction and Building Materials, 2025, 458: 139531.
585 [9] Ewa Kapeluszna, Katarzyna Chrabąszcz. Mutual compatibility of superplasticizers
586 (PC, SNF), GAs (TEA, glycol) and C3A in Portland cement systems - Hydration,
587 rheology, physical properties and air void characteristics [J]. Construction and Building
588 Materials, 2023, 373: 130877.
589 [10] Ewa Kapeluszna, Łukasz Kotwica. The Effect of Various GAs on the Properties of
590 Cement and Its Compatibility with Acrylate-Based Superplasticizer [J]. Materials, 2022,
591 15(2): 614.
592 [11] Haoxin Li, Chao Xu, Biqin Dong, Qing Chen, Linan Gu, Xiaojie Yang, Weishan
593 Wang.Differences between their influences of TEA and TEA·HCl on the properties of
594 cement paste [J]. Construction and Building Materials, 2020, 239: 117797.

595 [12] F.S. Hashem, E. E Hekal, M.A. El Wahab. The influence of Triethanol amine and
596 ethylene glycol on the grindability, setting and hydration characteristics of Portland
597 cement [J]. International Journal of Petrochemical Science & Engineerin, 2019, 4(3):
598 81-88.
599 [13] Guangwei Liang, Dayou Ni, Haoxin Li, Biqin Dong, Zhenghong Yang. Synergistic
600 effect of EVA, TEA and C-S-Hs-PCE on the hydration process and mechanical
601 properties of Portland cement paste at early age [J]. Construction and Building
602 Materials, 2021, 272: 121891.
603 [14] Junyi Jiang, Baoju Liu, Jinyan Shi, Osman Gencel, Xiang An, Jiafeng Gao.
604 Synergistic effect of glycine and triethanolamine on mechanical properties and
605 permeability of cement mortar [J]. Journal of Building Engineering, 2022, 51: 104283.
606 [15] Jun Jiang, Zhengmao Ye, Jiaming Wu, Qingchun Yang, Quanliang Li, Xiangming
607 Kong. Impact of triethanolamine on the hydration of Portland cement in the presence
608 of high pozzolanic activity supplementary cementitious materials [J]. Cement and
609 Concrete Composites, 2024, 147: 105435.
610 [16] Yazhou Zhao, Zhenyu Zhu, Yang Chen, Shagang Li, Yue Zhao, Xiaoyu Li, Min
611 Wu, Da Chen. Effect of TEA·H3PO4 and TEA·C18H30O3S on the mechanical
612 properties and hydration characteristics of cement paste [J]. Construction and Building
613 Materials, 2022, 314: 125635.

614 [17] Tamino Hirsch, Zichen Lu, Dietmar Stephan. Impact of triethanolamine on the
615 sulfate balance of Portland cements with mixed sulfate carriers [J]. Journal of the
616 American Ceramic Society, 2021, 104: 4829-4842.
617 [18] Jianguo Han, Kejin Wang, Jiyao Shi, Yue Wang. Mechanism of triethanolamine on
618 Portland cement hydration process and microstructure characteristics [J]. Construction
619 and Building Materials, 2015, 93: 457-462.
620 [19] Yanrong Zhang, Xiangming Kong, Zichen Lu, Zhenbao Lu, Qing Zhang, Biqin
621 Dong, Feng Xing. Influence of triethanolamine on the hydration product of portlandite
622 in cement paste and the mechanism [J]. Cement and Concrete Research, 2016, 87: 64-
623 76.
624 [20] Vincent Hallet, Tobias Hertel, Lies Eykens, Nele De Belie, Yiannis Pontikes.
625 Alkanolamines as GAs and hydration enhancers in blended cements with iron-rich non-
626 ferrous metallurgy slag [J]. Construction and Building Materials, 2025, 470: 140575.
627 [21] J.C.O. Zepper, S. de Bruin, X. Ling, K. Schollbach, S.R. van der Laan, H.J.H.
628 Brouwers. Improving the early reactivity of activated basic oxygen furnace slag - The
629 influence of particle fineness and Gas [J]. Journal of CO_2 Utilization, 2024, 83: 102821.
630 [22] Yiqie Dong, Xiyi Ning, Tianyu Han, Haobo Hou, Meng Zang, Haijun Lu, Xuyang
631 He.Triethanolamine assisted ball milling activation of high alumina fly ash: Grinding
632 kinetics, activation mechanism [J]. Ceramics International, 2025, 51(4): 4168-4177.
633 [23] Wei Jingli, Li Shuyang, Chen Zheng, Su Junchi, Zhao Jie. Multi-factor Model and
634 Microscopic Mechanism of Strength of Sugarcane Bagasse Ash Mortar based on

635 Particle Characteristics Regulation [J]. Journal of Building Materials, 2024, 27(5): 418-
636 424.
637 [24] Liu Bao, Pan Ganghua, Gao Min, Meng Haining. Influence of grinding aid on the
638 grinding effect of iron tailings and hydration properties of blended cement [J]. Journal
639 of southeast university (Natural Science Edition), 2022, 52(5): 907-916.
640 [25] Zhao Jihui, Dongmin Wang, Peiyu Yan, and Wenping Li. Comparison of Grinding
641 Characteristics of Converter Steel Slag with and without Pretreatment and Gas [J].
642 Applied Sciences, 2016, 6(11):237.
643 [26] Yibiao Teng, Songhui Liu, Zhaocai Zhang, Jiangwei Xue, Xuemao Guan. Effect
644 of triethanolamine on the chloride binding capacity of cement paste with a high volume
645 of fly ash [J]. Construction and Building Materials, 2022, 315:125612.
646 [27] Yan He, Shuhua Liu, Xiong Zhang, Wenbin Liu, Gaoyu Liao, Mingfeng Xu.
647 Influence of triethanolamine on mechanical strength and hydration performance of
648 blended cement containing fly ash, limestone and slag [J]. Journal of Building
649 Engineering, 2021, 44: 102879.
650 [28] Liu Zhiwei, Lu Zichen, Zhang Liheng, Pan Ye, Sun Zhenping. Effect of
651 Triethanolamine on Hydration and Sulfate Balance of Metakaolin Blended Cement [J].
652 Journal of building materials, 2024, 27(06): 528-535.
653 [29] Wang Sheng, Mei Junpeng1, Xie Jiacheng, Chen Yichun1, Dai Junjie. Influence
654 of Triisopropanolamine on Mechanical Properties and Hydration Characteristics of
655 Cement-Steel Slag System [J]. Journal of building materials, 2024, 27(11): 977-984.

656 [30]Jixiang Wang, Le Han, Ze Liu, Dongmin Wang. Setting controlling of lithium slag-
657 based geopolymer by activator and sodium tetraborate as a retarder and its effects on
658 mortar properties [J]. Cement and Concrete Composites, 2020, 110: 103598.
659 [31] Zhou Xianliang, Dai Wei, Zhu Xi, Zhou Xiaojun. Study on the Impact of Lithium
660 Slag as an Alternative to Washed Sand on Mortar Properties [J]. Materials, 2025, 18(15):
661 3490.
662 [32] Shuangkuai Dong, Shengwen Tu, Liangliang Chen, Liangliang Chen, Fufei Wu,
663 Lilan Xie, Qi Zhuo, Songhan Yu. Investigation of the performance of cement mortar
664 incorporating lithium slag as a super-fine aggregate [J]. Frontiers in Materials, 2023,
665 10: 1134622.
666 [33] Zhi Chen, Sili Chen, Liwen Li, Yuwan Zhou. Effects of Lithium Slag on the Frost
667 Resistance of Cement-Soil [J]. Materials, 2022, 15(16): 5531.
668 [34] Jiongfeng Liang, Wanjie Zou, Yongliang Tian, Caisen Wang, Wei Li. Effect of high
669 temperature on mechanical properties of lithium slag concrete [J]. Scientific reports,
670 2024, 14(1): 11872.
671 [35] Yingda Zhang, Zhaopeng Tang, Xianliang Zhou, Yantao Zheng, Zihao Liu. Effect
672 of alkali activator and granulated blast furnace slag on the properties of lithium slag-
673 based high-strength lightweight aggregates [J]. Scientific Reports, 2025, 15(1): 30115.
674 [36] Can Li, Jun Li, Wenqiang Chen, Zhongyuan Lu, Binxin Zhan, Fengyuan Yang, Li
675 Hou, Xuemei Chen, Qinghua Yu, Wen Zhong, Chen Jiakun, Jun Jiang. Performance and

676 hydration of ternary compound cement by using lithium slag, limestone and clinker [J].
677 Case Studies in Construction Materials, 2025, 22: e04435.
678 [37] Xun Wang, Yichen Shan, Shiyu Zhuang, Qiang Wang. Design of a novel all-solid
679 waste cementitious system based on lithium slag: Mechanical properties, hydration
680 mechanisms, and economic-environmental performance [J]. Construction and Building
681 Materials, 2025, 490: 142579.
682 [38] Zhang Jixiu, Sun Henghu, Wan Jianhua, Zhang Na.^{29}Si polymerization degree of
683 hydrates in coal gangue added cement [J]. Journal of Central South University (Science
684 and Technology), 2011, 42(2): 329-335.
685 [39] Wang Yan, Zhu Yimin, Xie Ruiqi, Cheng Zhouyueyang, Li Yanjun. Crystal
686 chemical genes characteristics of albite and prediction of its floatability [J]. Metal Mine,
687 2020, (06): 81-86.
688 [40] Changlong Wang, Yang Qi, Jianlin Jing, Jintao Ma, Yongxiang Zhou, Haoyan Ping,
689 Yongchao Zheng, Yuxin Zhai, Feng Liu. Properties and microstructure of total tailings
690 cemented paste backfill material containing mining and metallurgical solid waste [J].
691 Frontiers in Earth Science, 2023, 11: 1181952.
692 [41] Zichen Lu, Xiangming Kong, Daniel Jansen, Chaoyang Zhang, Jian Wang,
693 Xiaofan Pang, Jianhao Yin. Towards a further understanding of cement hydration in the
694 presence of triethanolamine [J]. Cement and Concrete Research, 2020, 132: 106041.

695 [42] Lian Huizhen, Shi Haixia. Clarification of a hypothesis on 'centroplasm of cement-
696 based composite' proposed by Wu Zhongwei [J]. Journal of the Chinese Ceramic
697 Society, 2020, 48(5): 777-786.
698